Quantitative analysis of electro-anatomical maps: application to an experimental model of LBBB/CRT

David Soto-Iglesias, Nicolas Duchateau, Constantine Butakoff, David Andreu, Juan Fernández-Armenta, Bart Bijnens, Antonio Berruezo, Marta Sitges, Oscar Camara

▶ **To cite this version:**

David Soto-Iglesias, Nicolas Duchateau, Constantine Butakoff, David Andreu, Juan Fernández-Armenta, et al.. Quantitative analysis of electro-anatomical maps: application to an experimental model of LBBB/CRT. IEEE Journal of Translational Engineering in Health and Medicine, 2017, 5, pp.1900215. ⟨10.1109/JTEHM.2016.2634006⟩. ⟨hal-01398828⟩

HAL Id: hal-01398828

https://inria.hal.science/hal-01398828v1

Submitted on 17 Nov 2016

HAL is a multi-disciplinary open access archive for the deposit and dissemination of scientific research documents, whether they are published or not. The documents may come from teaching and research institutions in France or abroad, or from public or private research centers.

L'archive ouverte pluridisciplinaire **HAL**, est destinée au dépôt et à la diffusion de documents scientifiques de niveau recherche, publiés ou non, émanant des établissements d'enseignement et de recherche français ou étrangers, des laboratoires publics ou privés.

HAL Authorization

Preprint version accepted to appear in IEEE Journal of Translational Engineering in Health and Medicine.
Final version of this paper available at http://ieeexplore.ieee.org/xpl/RecentIssue.jsp?punumber=6221039

Quantitative analysis of electro-anatomical maps: application to an experimental model of LBBB/CRT.

Soto-Iglesias D., Duchateau N., Butakoff C., Andreu D., Fernández-Armenta J., Bijnens B., Berruezo A., Sitges M. and Camara O.

Abstract Electroanatomical maps (EAMs) are commonly acquired in clinical routine for guiding ablation therapies. They provide voltage and activation time information on a 3D anatomical mesh representation, making them useful for analyzing the electrical activation patterns in specific pathologies. However, they are extremely acquisition dependent and complex, and therefore difficult to quantify and compare with other EAMs acquired at different times or from different patients. In this paper, we introduce a set of tools for the quantitative analysis of EAMs, going beyond the methods currently used in clinical practice. They are based on the quantitative estimation of simple biomarkers relevant to disease and therapies. Notably, we develop global indices (total activation time), local indices (local activation time, surrogates of conduction velocity, inter-ventricular and transmural delays), and therapy-based indices (lead position) to better characterize EAM data. Furthermore we propose 2D and 3D representations of the activation patterns –for their enhanced visualization and comparison in a common reference system. After verification and validation experiments on synthetically generated data, the proposed analysis tools are applied to EAM data obtained in an experimental swine model of induced Left Bundle Branch Block (LBBB) with an implanted Cardiac Resynchronization (CRT) device. Specifically, we have analyzed and compared electrical activation patterns at baseline, LBBB and CRT stages in 4 animals: two without any structural disease; and two with an induced infarction. The proposed tools automatically relate the ventricular lead location with electrical dyssynchrony, which allows evaluating the current hypothesis about lead placement in CRT.

***Index Terms*— Cardiac resynchronization therapy; electro-anatomical mapping system; quantitative pattern analysis; left bundle branch block; subject-specific 2D and 3D data representation; lead placement.**

I. INTRODUCTION

In this paper, we target the assessment of changes in the electrical activation of the heart, which is of prime importance to better understand the pathophysiological mechanisms in cardiac diseases. Qualitative and quantitative evaluation of electrical pattern changes is feasible, but requires specific tools to consider the anatomical and functional variability of these data.

Electro-anatomical maps (EAMs), acquired with electrophysiological mapping system are well established in daily clinical routine. They are mainly used for guiding radio-frequency ablation (RFA) for the treatment of different arrhythmias [1]. EAMs are reconstructed from the processing of intracardiac electrograms acquired through the contact of a catheter with the endo- or epi-cardial walls together with catheter tracking, which results in a discrete set of points where electrical and anatomical information is available. As a result an anatomical mesh is obtained with electrical activation indices associated to its nodes (see Figure 1a). This joint information helps to qualitatively analyze changes in electrical patterns under different conditions, such as in the presence of a left bundle branch block (LBBB) [2] and when a Cardiac Resynchronization Therapy (CRT) has been implanted [3]. However, EAMs are difficult to compare because they are extremely dependent on different factors like patient anatomy as well as the number, location and accuracy of the acquired points. These differences and uncertainties in EAM measurements make the analysis of EAM electrical patterns highly challenging. At the time being, clinicians usually perform a visual assessment of the electrical activation patterns [2, 4], which is complemented by basic global indices such as the total activation time (TAT), or the QRS length provided by ECG and EAM data. Slightly more sophisticated analysis of electrical patterns have also been proposed [5, 6], based on simple indices (e.g. area and anisotropy) estimated on local activation time (LAT) isochrones extracted from EAMs. More advanced computational techniques are commonly applied to combine multi-modal information from the same patient to guide RFA interventions. For instance, structural and tissue information from pre-operative imaging data (e.g. Magnetic Resonance Imaging, MRI or Computed

This study was partially founded by the Spanish Ministry of Science and Innovation (TIN2011-28067) and the Spanish Industrial and Technological Development Center (cvREMOD-CEN-20091044).

DSI, CB, BB and OC are with PhySense, DTIC, Universitat Pompeu Fabra, Barcelona, Spain (e-mail: david.soto@upf.edu).

BB: ICREA.

ND is with Asclepios Research project, Inria Sophia Antipolis, France.

DA, JFA, AB and MS are with Cardiology Department, Thorax Institute, Hospital Clinic, Barcelona, Spain.

Preprint version accepted to appear in IEEE Journal of Translational Engineering in Health and Medicine. Final version of this paper available at http://ieeexplore.ieee.org/xpl/RecentIssue.jsp?punumber=6221039

Tomography, CT) can be fused with EAM data with basic registration algorithms based on landmarks in atrial fibrillation and ventricular tachycardia [7, 8, 9, 10, 17]. The main drawback of these techniques is that they cannot easily be applied to analyze and compare EAM data acquired at different time-points or from different patients due to the lack of a common reference system.

Several researchers have proposed computational techniques to construct 2D reference systems for different organs such as, the atria [12, 13], the brain [14, 15], the liver [16], the cochlea [17], vertebral bones [18] or faces [19] that allow inter- and intra-patient comparisons. We recently developed a planar disk representation where the left ventricle (LV) of the heart is quasi-conformally mapped by flattening [20, 21] and this was applied to EAM and delay-enhancement magnetic resonance imaging (DE-MRI) data. Once the EAMs are standardized into a common reference frame, they can be analyzed and compared, both qualitatively and, more important, quantitatively. Nevertheless, classical statistics, which may be used on electrical patterns that are coherent within a population [22], are not relevant in case of e.g. the presence of pacing leads or localized infarcts due to the heterogeneity of the samples. More relevant indices extracted from EAMs are therefore required to overcome these limitations.

In this paper we propose a methodology to study EAMs that addresses the two following challenges: (i) definition of a reference system for EAMs of the two ventricles of the heart (LV and right ventricle, RV); and (ii) quantitative analysis of electrical pattern changes. The algorithm is based on our previous work [20, 21] which only worked on LV endocardial data. Here, the methodology is extended to include epicardial EAM data from both ventricles (see Figure 1.b), in a way that allows generating activation histograms for an inter- (RV/LV epicardium) and intra-cavity (transmural) analysis, which provide valuable clinical information on electrical dyssynchrony [23]. The 2D disk representation of the reference common system is frequently used in clinical cardiology when displaying LV endocardial data on a bull's eye plot (BEP) [24] and it is appropriate for identifying the electrical propagation pattern. However, it does not provide intuitive insight about the speed of the electrical wave, which is important for a complete understanding of the heterogeneous EAM patterns, e.g. including the Purkinje system. Therefore, we also introduce a new 3D BEP representation extending the 2D BEP so that every point is elevated proportionally to its corresponding LAT value (see Figure 1.c).

The developed analysis tools are illustrated in the context of CRT, which is a treatment used to improve cardiac pump function in patients with heart failure by synchronizing heart contraction. However, the high rate of non-responders (around 30%) and the associated costs are still of primary concern [25, 26]. In order to optimize CRT some studies aimed at identifying the best configuration of the device, including lead positioning [27, 28, 29, 30, 31], which has also been investigated with in-silico experiments [32, 33]. Despite these advances, patient selection and CRT optimization is still under debate, since the underlying mechanisms of LBBB and CRT are not fully understood.

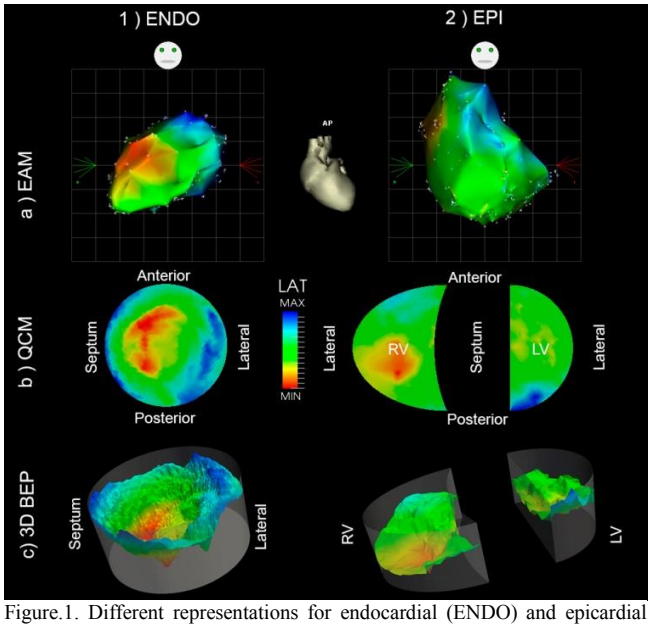

Figure.1. Different representations for endocardial (ENDO) and epicardial (EPI) electrical activity. a) Classical electro-anatomical maps (EAMs) meshes from the mapping system; b) 2D flattening of the left (LV) and right (RV) ventricles with a quasi-conformal mapping technique; c) 3D representation of the flattened disk that allows to relate electrical activation times with conduction velocities (altitude gradient). Colors represent local activation times (the maximum and minimum values were not specified since this figure is only used for illustrative purposes).

In this paper, these mechanisms are studied, both qualitatively and quantitatively, by applying the developed computational tools on endocardial and epicardial EAM data of the LV and RV acquired on an experimental swine model of induced LBBB with an implanted CRT device. Different indices are estimated regionally (e.g. endo-epi, RV-LV) such as the total activation time (TAT) recovery, the inter-ventricular delay (IVD) and the LV transmural delay (LV-TD) after CRT implantation. These indices are then related to other clinical information such as lead positioning or the presence and localization of myocardial infarcted tissue. Previously, verification and validation experiments are performed on synthetic and fully controlled data.

II. METHODS

Our main goal is to extract indices to better analyze and compare electrical patterns in EAM data from biventricular surfaces of cardiac chambers. To that end we propose an integrated 2D disk representation (2D BEP) of the LV and RV obtained with a quasi-conformal mapping from the 3D EAM meshes. Electrical wave propagation is then studied deriving speed maps from LAT values in the 2D BEP and by extending this representation to 3D (3D BEP). In addition, we compute histograms of the activation to identify electrical heterogeneities in different regions of the heart. These representations allow the estimation of therapy-related parameters such as CRT lead positioning and related them to global and local indices characterizing changes in electrical activation patterns such as TAT recovery, inter-ventricular and transmural delays.

Preprint version accepted to appear in IEEE Journal of Translational Engineering in Health and Medicine. Final version of this paper available at http://ieeexplore.ieee.org/xpl/RecentIssue.jsp?punumber=6221039

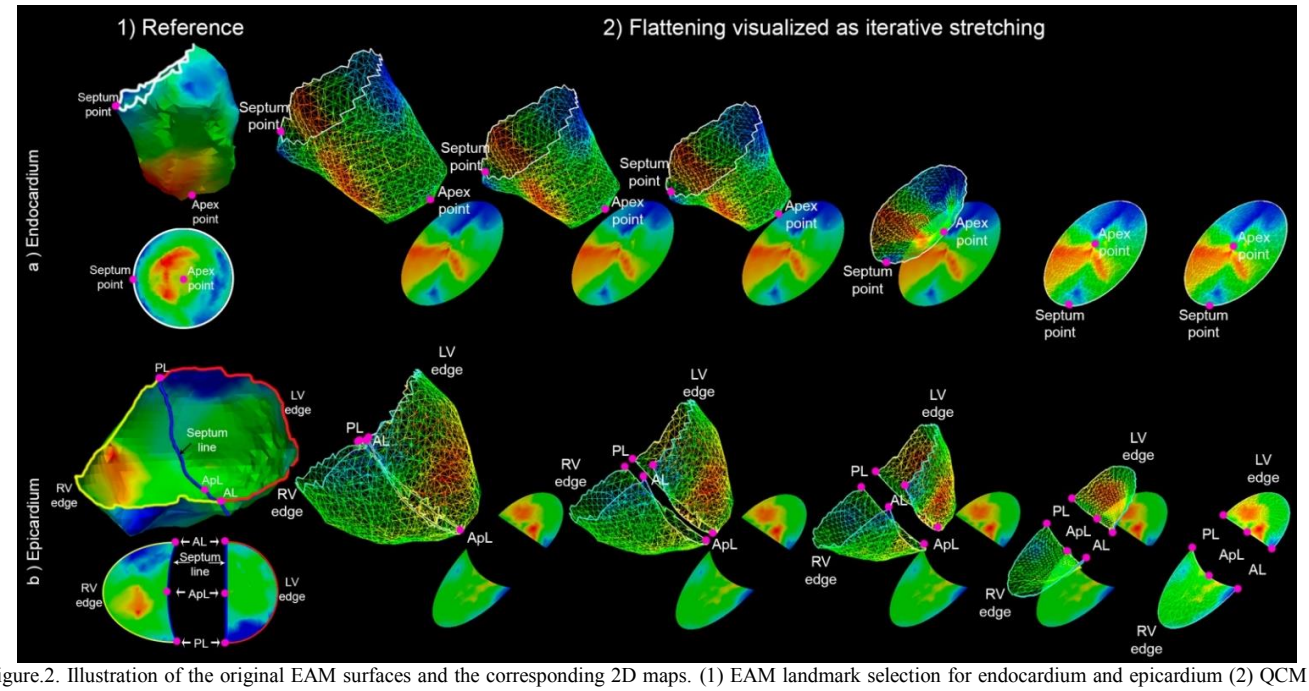

Figure.2. Illustration of the original EAM surfaces and the corresponding 2D maps. (1) EAM landmark selection for endocardium and epicardium (2) QCM sequence for endocardial and epicardial EAMs illustrating the correspondence; the selected landmarks are also show: Posterior landmark (PL), anterior landmark (AL), apical landmark (ApL).

A summary of the proposed indices together with their purpose is included in Table S1 on the supplementary material.

A. 2D disk representation of left and right ventricles.

The 2D disk representation (2D BEP) is obtained following the methodology we presented in Soto-Iglesias et al. [4, 5] on the LV endocardium. Here we analyze not only data from the LV endocardium (EAM measurements from the RV endocardium are not available) but also from the RV and LV epicardium. Firstly, we compute a vanishing conformal Laplacian that smoothly maps every vertex of the 3D EAM mesh to a 2D disk [20, 21]. In order to get a unique solution, we need to impose some boundary conditions and identify two landmarks. Initially, the boundary points of the 3D mesh must be mapped into the circumference of the 2D disk, preserving the 3D relative distance between them. We also force the mapping to follow the 17 AHA segments definition, thus a point in the middle of the septum (Septum point in Figure 2a) is placed at the (-1, 0) XY coordinates of the disk. After the mapping, the apex is displaced to the center of the disk (0, 0) by applying thin plate splines (TPS) transformation, which results in a quasi-conformal mapping (QCM), as illustrated in Figure 2a.

The representation of the epicardium was established in a similar way. However, the epicardium is not mapped into a 2D disk since both ventricles share it, which may be misleading when compared to endocardial data. We then choose to map LV and RV data to separate half disks, as in [23]. Firstly, the septum line (SL) is defined on the 3D EAM mesh. To do so, three landmarks are manually selected (Figure 2b): one at the apex of the epicardium, and two in the boundary of the mesh, specifically on the posterior (posterior landmark PL) and anterior (anterior landmark AL) edges. In the 3D mesh the SL is then defined as the geodesic line that connects the PL and AL landmarks and goes through the septum. In the 2D space the LV is defined as (the right) half of a disk. In order to be consistent with the endocardial mapping, the AL and PL landmarks are located at the (0, 1) and (0, -1) XY coordinates. The 2D septum line is then defined as the line that joins these two landmarks, while the LV lateral wall boundary is forced to the contour of the half (right) disk. A similar approach is applied for mapping the RV epicardial EAM onto a half-moon shape.

An additional difficulty is that each EAM has a different number of acquired points. Thus, the data mapped onto the 2D BEP must be reparameterized to compare different EAMs. A common set of nodes is generated as intersection points between 50 equidistant concentric circles of increasing radius with 300 rays emanating from the center of the disk, resulting in 15000 nodes with a resolution of 0.02 x 0.02 in polar coordinates. Information associated to the EAM points is then transferred to the new nodes using linear interpolation and barycentric coordinates.

B. Histograms of activation

A complementary type of representation for EAM data based on histograms computed from local activation times was developed. These histograms are built for endocardial and epicardial data and characterize the distribution of the data depending on the time of activation of every point. The total activation time (TAT), which is defined as the difference between the earliest and latest activation points, is divided in a certain number of intervals, so-called

Preprint version accepted to appear in IEEE Journal of Translational Engineering in Health and Medicine. Final version of this paper available at http://ieeexplore.ieee.org/xpl/RecentIssue.jsp?punumber=6221039

isochrones in clinical terms or bins in statistics, which represent the percentage of the tissue activated within a certain TAT interval. We have divided the TAT into 20 bins, corresponding to intervals of 5%, since it provided enough resolution for the studied phenomena. Examples of these histograms are given in all remaining figures of the paper. The main advantage of this data representation is that it shows very intuitively (electrical) dyssynchrony and heterogeneities between different parts of the heart (e.g. endo-epi, RV-LV).

C. Speed maps

As described above, the 2D disk representation is parameterized as the intersection of concentric circles with emanating rays at different angles, which allows working in polar coordinates. Each ray angle and concentric circle represents the Θ and r polar coordinates, respectively. Our surrogate for the speed of conduction is then computed as follows:

$$Speed_{(r,\theta)} = \frac{1}{\| \nabla LAT_{(r,\theta)} \|} \quad (1)$$

$$\nabla LAT_{(r,\theta)} = \frac{\partial LAT}{\partial r} e_r + \frac{1}{r}\frac{\partial LAT}{\partial \theta} e_\theta, \quad (2)$$

where $\nabla LAT_{(r,\Theta)}$ corresponds to the gradient of the local activation time (LAT), and it is computed on the 2D disk in polar coordinates as in Equation 2. In practice, $\nabla LAT_{(r,\Theta)}$ is estimated using finite differences. In order to minimize the speed map noise, a Gaussian low-pass filter (h=11/ σ=2) is applied. These speed maps are very convenient to distinguish regions with different conduction velocities such as fast activation due to the Purkinje system (PK) (i.e. electrical pathways with velocities around 2-4 times higher than working myocardial tissue) or slow conduction due to a block of activation induced by the presence of scar. An automatic classification of different regions in the speed maps is then performed applying the k-means algorithm (k=4) [34]. This classification algorithm is simultaneously applied to the speed maps at baseline, LBBB and CRT, resulting in 4 different clusters, which allows a direct comparison of these maps (Figure 3). On the other hand, LAT-related data are independently normalized (e.g. max and min definitions in colormaps) for every stage (baseline, LBBB and CRT) due to the large differences in LAT ranges between them (see TAT values in Figure 6).

D. 3D BEP Representation of the heart

The 2D speed maps represented above complement the 2D BEP maps by adding visual information on electrical propagation speeds. Here we introduce another representation of LAT data, in the form of 3D BEP maps that also help to identify regions with different activation speeds. Remember that the vertices of the 2D BEP are located on the XY plane and that a LAT value is associated to each of them. We normalize the LAT values of each map (independently) to lie between 0 (minimum, earliest activation) and 1 (maximum, latest activation).

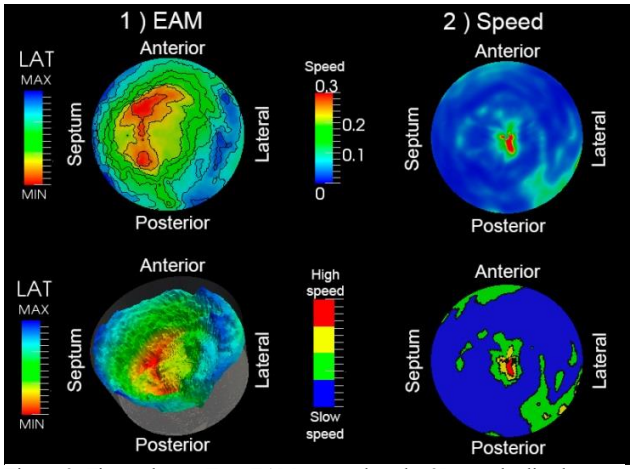

Figure.3. First column: Top, EAM mapped to the 2D standardized space; bottom, 3D BEP representation, from the earliest activation (red) to the latest one (blue); Second column: Top, speed map; bottom, speed classification using k-means, form the slowest velocities (blue) to the highest ones (red).

In order to incorporate speed information, we assign the normalized LAT to the z coordinate of each vertex. In this 3D representation, low values of z indicate earliest activated points, while high values represent the latest activated ones. Therefore, in a very intuitive way, a block in electrical conduction is visualized in these 3D BEP maps as a region with a steep slope (e.g. a mountain corresponding to a high gradient in LAT values) while a high-speed conduction area is visualized as a flat zone.

E. Global and local quantitative indices

From the EAM representations described above, we compute a set of global and local indices characterizing the electrical pattern changes and some parameters related to the therapy (i.e. CRT).

1) Indices on electrical pattern changes

a) Total activation times (TAT)

Total activation times (TAT) are computed as the difference between the earliest and latest activated points, considering both endocardial and epicardial EAM data. Differences (Δ) between baseline, LBBB and CRT stages are then evaluated as follows:

$$\Delta_{base} = TAT_{base} - TAT_{LBBB} \quad (3)$$

$$\Delta_{CRT} = TAT_{LBBB} - TAT_{CRT} \quad (4)$$

$$TAT_{Recovery} = \frac{\Delta_{CRT}}{\Delta_{base}}.100, \quad (5)$$

where $\Delta base$ represents the delay induced by LBBB (with respect to baseline), ΔCRT is the effect of CRT (i.e. difference in TAT between CRT and LBBB stages) and the $TAT_{recovery}$ indicates how close TAT is to baseline after applying CRT.

Preprint version accepted to appear in IEEE Journal of Translational Engineering in Health and Medicine. Final version of this paper available at http://ieeexplore.ieee.org/xpl/RecentIssue.jsp?punumber=6221039

b) Inter-ventricular and transmural delays

Histograms of activation allow the estimation of indices characterizing the electrical dyssynchrony by comparing isochronal (or bin) distributions corresponding to different regions of the heart. Hence we evaluate RV/LV and transmural (endo-epi) synchronization computing distances between the starting and ending bins at each stage of the protocol (baseline, LBBB and CRT). The two resulting indices are: (i) the inter-ventricular delay (IVD), which is defined as the temporal difference (in milliseconds) between the epicardial RV and LV starting bins; (ii) The LV transmural delay (LV-TD), which is defined as the temporal difference (in milliseconds) between the endocardial and epicardial LV starting bins. An equivalent transmural delay could be computed for the RV if data were available.

c) Speed index

The speed maps allow extracting quantitative indices to further characterize electrical propagation in the four different speed clusters, enabling to compare them regionally at each stage (baseline, LBBB and CRT). Here, we define a simple speed index as the percentage of tissue within each speed cluster. Additionally speed maps are also qualitatively analyzed to recognize areas of slow of block of conduction due to scar or between the two ventricles.

2) Therapy-related indices

a) Lead location

We use the 2D BEP representation of EAM data to automatically identify the CRT leads in the ventricles. Although the most common CRT configuration is based on the implantation of one lead at the apical region of the RV endocardium and another one at the LV lateral wall, the optimal LV lead position is highly controversial [27, 28, 29, 30, 31]. Once the CRT device is operating, leads control the electrical activation at every heartbeat, to (as in our experiments) impose a zero-delay between the shocks from both leads and then force a synchronous activation between the septal and lateral walls of the LV. Hence we select the nodes within the first 10 ms of electrical activation to detect the CRT leads in the 2D BEP. As a result there are two distinguishable clouds of points (whose centers correspond to lead locations) that are automatically detected with a simple k-means classification algorithm [34] (k=2). The localization of the RV lead is estimated on the epicardial EAM data since we do not have measurements from the endocardial RV. Therefore, the resulting localization mainly represents the epicardial breakthrough (BT) induced by the endocardial RV lead rather than its exact location. Nevertheless, the myocardium is relatively thin at the apical RV, thus we consider activation time differences between the endocardial and epicardial RV to be negligible comparing to the LAT range in the two ventricles.

b) Lead apicality index

The 2D BEP represents the EAM data in a disk, where apical positions are at its center and basal ones are close to its circumference (radius equal to zero and to one in polar coordinates, respectively). In this way, the distance from any 2D BEP point to the center of the disk corresponds to its distance to the apex. The *apicality index* is then defined as $1 - r$, where r represents a normalized version of this distance – since we map the EAM to an unitary disk, all distances are normalized according to a vanishing conformal Laplacian– so that values lie with the [0, 1] interval (close to zero or one if the point is basal or apical, respectively). The apicality index is then computed for each lead location, estimated as described above, providing a quantitative measure with a common reference system to compare lead positioning in different EAM data.

c) Lead distance indices

Defining the optimal LV lead placement is a challenging task with different possible approaches. In [27], the authors suggested avoiding apical positions while other studies [35, 36] proposed the latest mechanical activation area in LBBB as the optimal target for improving the CRT effect.

In order to test these hypotheses we define two geodesic distance indices involving the LV lead positioning: (i) geodesic distance between the RV and LV leads; and (ii) geodesic distance between the LV lead placement in CRT and the latest electrically activated zone (LAZ) in LBBB (considering it a good approximation of the latest mechanically contracting area).

To compute geodesic distances on the 2D BEP is not possible since these are not exactly preserved after the quasi-conformal mapping. Additionally the original EAM mesh can neither be used for this purpose due to its low resolution and high noise level (see Figure 1a). In order to have an approximation of the LV lead-related geodesic distances we used a high-resolution mesh built from the LV geometry of a non-infarcted pig, which is segmented from MRI. This high resolution LV mesh is then taken as a reference surface for all cases, which is mapped to the 2D BEP and the EAM data with the QCM mapping technique to establish correspondences between the data, as we proposed in [21].

For computing the geodesic distance between LV lead and the latest activated area in LBBB, we need to define the latest activation area in the LBBB 2D representation map. To do so, the latest activation point in LBBB is defined as the center of the point cloud corresponding to the last 10ms isochrone. Then, the geodesic distance is computed by projecting it onto the 3D MRI surface.

Preprint version accepted to appear in IEEE Journal of Translational Engineering in Health and Medicine. Final version of this paper available at http://ieeexplore.ieee.org/xpl/RecentIssue.jsp?punumber=6221039

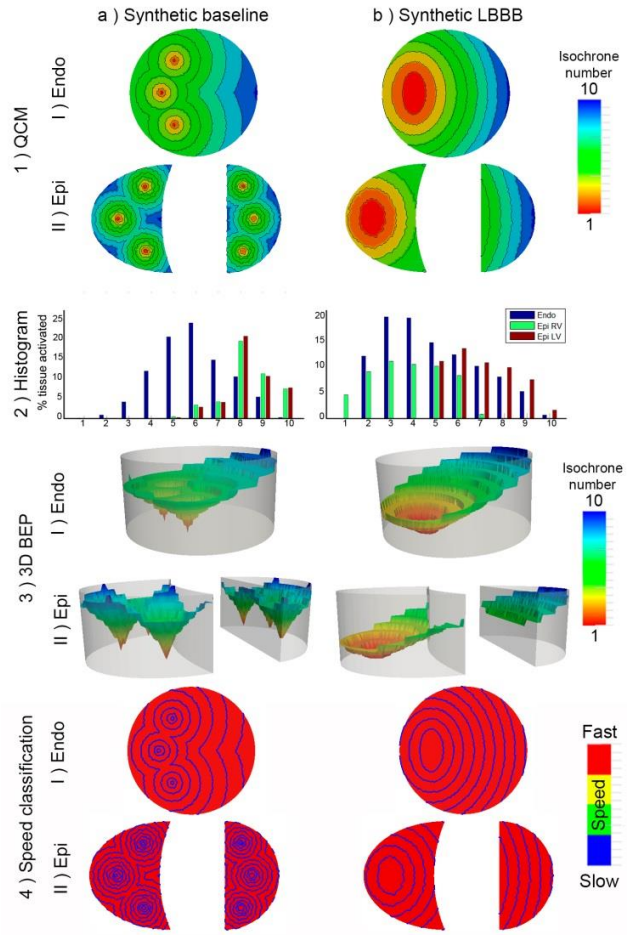

Figure 4. Synthetic activation patterns: a) Circular activation pattern (baseline) b) Elliptical activation pattern (LBBB); 1) 2D BEP for endocardium and epicardium from the earliest activation (red) to the latest one (blue); 2) Histogram of isochrones for LV/RV epicardium and LV endocardium (RV endocardium is not available); 3) 3D BEP for endocardium and epicardium from the earliest activation (red) to the latest one (blue); 4) Speed maps for endocardium and epicardium for slow speeds (blue) and fast speeds (red).

III. RESULTS ON SYNTHETIC DATA

Two synthetic activation patterns simulating normal and LBBB electrical activation have been developed for illustrating the limitations of a global analysis and the benefits of a detailed one on fully controlled data.

A. Generation of synthetic data

We generated the following two synthetic electrical activation patterns (see Figure 4): (i) a circular activation shape that simulates a normal (i.e. baseline) electrical activation pattern; and (ii) an elliptical activation shape that represents a LBBB electrical activation pattern. In order to emphasize the importance of an advanced and local analysis of the electrical activation patterns, the total activation time is forced to be the same (equal to 100 ms) for both synthetic examples. Electrical isochrones are generated as steps of 10% of the TAT, resulting in 10 isochrones.

1) Normal activation pattern

The normal activation pattern is characterized by growing concentric (i.e. isotropic) circles starting from different activation sites. A total of ten circles, whose radii are uniformly increased, correspond to the different isochrones completing the whole activation pattern. The influence of the three main branches of the Purkinje system (PS) on the LV endocardial activation pattern at baseline is introduced with three different early-activated sites in the LV septal wall (red in Figure 4a). Since at baseline both RV and LV bundle branches of the PS are healthy, both ventricles are simultaneously activated at the epicardium. Therefore, a total of six sites are chosen as initial activation points at the epicardium, three of them in each ventricle.

2) LBBB activation pattern.

In LBBB the LV electrical activation pattern comes from the RV (through the septum) since the left bundle branch of the PS is not functioning. Therefore, we set the first activation isochrone to start only at one site and it presents a larger area than in baseline. In consequence, the LBBB endocardial activation pattern is defined with ten isochrones starting from one point located at the middle of the LV septum and linearly increasing the radii of the ellipses in equal steps. The RV epicardium is activated before than the LV one due to the LBBB of the PS, and it follows a similar activation pattern than the LV endocardium. The epicardial map is then activated as the LV endocardium but with starting and ending in the RV and LV epicardium, respectively (Figure 4.1b).

B. Activation pattern analysis on synthetic data

Firstly, it needs to be pointed out that the two synthetic activation patterns described above provide the same total activation time, which is the only index currently used to quantitatively analyze EAM data, even though they have very different electrical patterns. On the other hand the histogram of isochrones (Figure 4.2) clearly reveals the amount of inter-ventricular and LV transmural dyssynchrony present within each pattern. In the normal case (Figure 4.2a), it can be seen how the activation pattern starts slowly at the endocardium. Then, its conduction velocity increases until bin #6, where the 25% of the nodes are activated. Subsequently the amount of activating tissue decreases with time. The activation reaches the epicardium from bin #5 (representing 50% of TAT) and then the LV and RV are synchronously activated. However, the histogram of the LBBB activation pattern shows a different sequence of activation: the earliest activated area in both ventricles is located in the RV epicardium; it is followed by LV endocardial activation; and it ends with the LV epicardium. In the epicardium, the percentage of activating tissue in the LBBB pattern is more uniformly distributed along the different isochrones than on the normal one, which indicates more uniform conduction velocities.

The 3D BEP representation shows the speed of propagation and the location of the earliest activated area (Figure 4.3). In the normal activation pattern, it initially shows a moderate steep slope from the earliest isochrones, which indicates a slow speed of propagation (working myocardium activation before reaching PS). Then, the central isochrones (green colors in Figure 4.3a) present a

Preprint version accepted to appear in IEEE Journal of Translational Engineering in Health and Medicine. Final version of this paper available at http://ieeexplore.ieee.org/xpl/RecentIssue.jsp?punumber=6221039

Pig	Recovery	LV-lead distances		Apicality index		Baseline Delays		LBBB Delays		CRT Delays	
#	%	LAZ (mm)	Leads (mm)	LV lead	RV lead	$LV\text{-}TD_{base}$ (ms)	IVD_{base} (ms)	$LV\text{-}TD_{LBBB}$ (ms)	IVD_{LBBB} (ms)	$LV\text{-}TD_{CRT}$ (ms)	IVD_{CRT} (ms)
1	47.7	15.2	73	0.19	0.95	6.6	-1.1	9.9	19.8	-6.6	-3.3
2	-2.6	65.3	22	0.79	0.89	15.3	11.9	7.2	18	0	7.3
3	100	22.5	35.3	0.50	0.68	22.5	2.25	-3.7	3.7	-6.75	0
4	342.9	17.4	37.5	0.33	0.35	31.2	0	11.8	17.7	-5.25	-12.25

Table 1. Quantitative and qualitative measures for: (i) two representative non-infarcted pigs (blue) and (ii) two representative infarcted pigs (orange). TAT:Total Activation Time; LAZ: latest electrically activated zone; LV and RV: left and right ventricle, respectively; LV-TD: LV transmural delay; IVD: inter-ventricular delay.

flatter area that indicates an increment of the speed of propagation (due to PS activation). Finally, the slope increases again in the last isochrones due to the reduction in the speed of propagation in this area (activation from PK terminals to working myocardium). A similar pattern can be appreciated in the epicardial activation on both ventricles.

On the other hand, the LBBB activation pattern produces a constant moderate slope in the endocardial 3D BEP (Figure 4.3b), indicating a more uniform velocity of propagation (only working myocardium activation without PS). At the epicardial 3D BEP (Figure 4.3b) it can be seen how the RV is activated significantly faster than the LV.

These differences between the two synthetic electrical activation patterns, which are independent of the total activation time, point out the limitation of a global analysis and the need for a deeper analysis.

IV. Results on Experimental Data

The developed set of tools has been applied to EAM data from an experimental swine model of LBBB and CRT. Specifically, this experiment demonstrates the relation between the CRT lead placement and the electrical resynchronization achieved after CRT by properly analyzing the electrical activation patterns.

A. Data acquisition protocol

A total of 4 representative pigs (average weight = 34 (30/35) kg) are studied in this paper, which are a sub-set of a larger database [37]. Two of them present a myocardial infarction located at the septal wall, whereas the other two do not have structural disease. A complete description of the whole dataset and its associated experimental protocol is given in [37]. Animal handling was approved by the Institutional Review Board and Ethics Committee at the Hospital Clínic, Barcelona, Spain, and conformed to international guidelines [38].

LBBB was induced in all animals using radio-frequency ablation, assisted by high rate pacing (160bpm) during the burning process to prevent ventricular fibrillation. All pigs were implanted with a RV apical lead (Beex RF45, Sorin Group, Milan, Italy) and a LV one (subxiphoid access or via coronary sinus, Situs OTW, Sorin Group). Pacing was performed with a pacing system analyzer (ERA-3000, Biotronik, Berlin, Germany), and optimized after the ablation procedure [39].

Contact mapping data were collected using an electro-anatomical mapping device (CARTO-XP, Biosense Webster, Diamond Bar, CA) after introducing a 3.5-mm tip catheter (Thermo-Cool Navi-Star, Biosense Webster Inc, Diamond Bar, CA, USA) through the femoral artery until reaching the endocardium of the LV (endocardial EAM) by the retrograde aortic access. Then, using the same catheter and system, an epicardial map of both ventricles was recorded. For this purpose, percutaneous pericardial access was obtained by a transthoracic subxiphoid puncture.

EAMs were subsequently generated by reconstructing information obtained from the set of sparse acquisition points where the clinician placed the catheter to measure the electrical activity (around 2500ms at 1 kHz). These electrical measurements were processed and rendered in 3D to display the local activation time for each point, as shown in Figure 1.1. The LAT is the parameter retained in the present study to investigate electrical activation patterns.

All EAM were acquired on the day of the experiment, at baseline, post-ablation (LBBB) and with CRT pacing, and the average number of points they contain were 171 ± 66 and 255± 76, for endocardium and epicardium respectively.

B. Activation pattern analysis on experimental data

The quantitative indices, introduces in Section II.E corresponding to the four analyzed pigs are summarized in Table 1.

1) Non-infarcted pig model

Pig #1 had leads implanted in the apical and basal regions for the RV and LV (apicality index of 0.19 and 0.95 respectively), which is arguably the optimal lead position. It achieved a TAT recovery of 47.7% and a quasi-complete biventricular resynchronization (IVD_{CRT} equal to -3.3ms), thus, it could be classified as a CRT responder. The fact that the $LV\text{-}TD_{CRT}$ is -6.6 ms indicates that the LV epicardium activates electrically 6.6 ms before the LV endocardium, which happens because the LV and RV leads are located on the epicardium and the endocardium, respectively.

Preprint version accepted to appear in IEEE Journal of Translational Engineering in Health and Medicine. Final version of this paper available at http://ieeexplore.ieee.org/xpl/RecentIssue.jsp?punumber=6221039

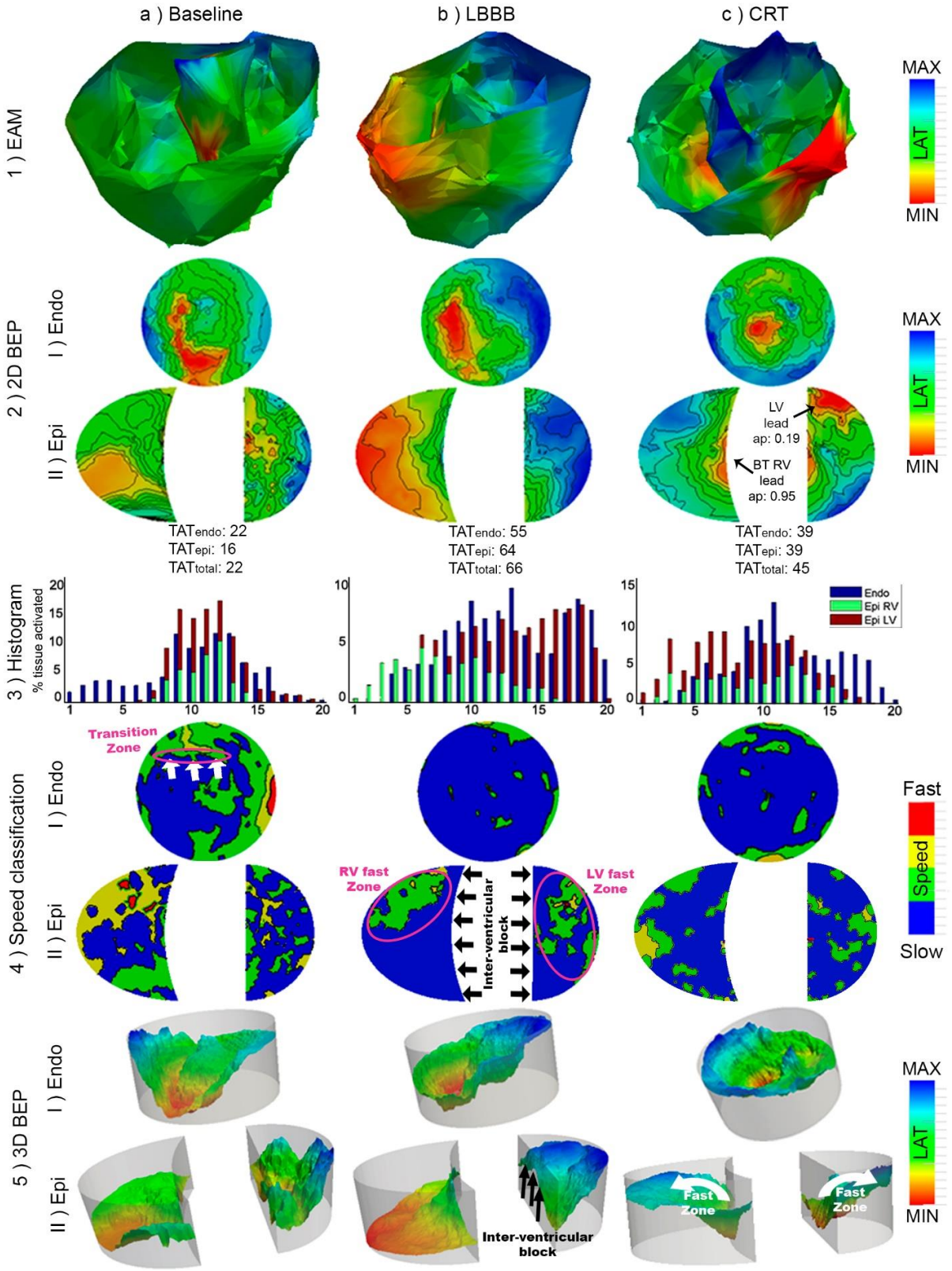

Figure 5. Non-infarcted case (*#1*). 1) Endocardial and epicardial EAMs 2) QCM of endo (LV) and epicardial (RV/LV) EAMs; BT RV: electrical breakthrough from the RV; 3) Histogram of isochrones (missing RV endocardium) 4) Speed classification from endo and epicardial velocity maps 5) 3D BEP from endo and epicardial QCM representations; Local activation time (LAT) values and speed scales are shown as min/max since they are different between each protocol stage.

Preprint version accepted to appear in IEEE Journal of Translational Engineering in Health and Medicine. Final version of this paper available at http://ieeexplore.ieee.org/xpl/RecentIssue.jsp?punumber=6221039

Pig	Endocardium												Epicardium											
#	Baseline				LBBB				CRT				Baseline				LBBB				CRT			
	High (%)			Low (%)	High (%)			Low (%)	High (%)			Low (%)	High (%)			Low (%)	High (%)			Low (%)	High (%)			Low (%)
1	0.9	3.8	45	**50**	0	0.3	8.8	**91**	0	1	16	**83**	3	24	50	**23**	0.1	3	24	**73**	2	4	17	**77**
2	2	8	26	**64**	0.5	1	19	**79**	0	0.1	2	**98**	2	15	53	**30**	0	0.2	13	**87**	0	0	10	**89**
3	0	0.6	12	**87**	1	4	11	**84**	0.1	3	21	**76**	1	12	42	**45**	0	2	22	**76**	0.7	4	28	**67**
4	1	6	32	**61**	1	10	21	**68**	2	9	38	**51**	0.3	3	36	**61**	0	0	6	**94**	0	0	10	**90**

Table 2. Percentages of endocardial and epicardial regions in each of the four speed clusters. Non-infarcted pigs (blue) infarcted (orange) pig experiments. High: fastest speed cluster; low: slowest speed cluster.

Figure 5 illustrates the electrical activation pattern of the CRT responder Pig #1. The 2D BEP representation (Figure 5.2) allows an easier and more intuitive electrical activation pattern analysis than with the 3D EAM (Figure 5.1). One can easily identify in the 2D BEP both the initial and final electrical activation zones (red and blue areas, respectively) and the propagation pattern at each stage (baseline, LBBB and CRT). It shows a homogeneous and faster activation of both LV endocardium and RV-LV epicardium at baseline compared to LBBB (Figure 5.2). It also shows three main spots of earliest activation (red areas in Figure 5.2a) that corresponds to normal Purkinje-based activation, which subsequently propagates to the muscle (transition between blue and green areas in the endocardial speed map, top left in Figure 5.4a), inducing an increment of the speed of conduction on the transition areas.

Visual inspection of the speed maps (Figure 5.4) and the speed indices (Table 2) reveal that Pig #1 presents a substantial increment of slow speed tissue (blue areas) after LBBB (from 50 % to 91% at endocardium), which is slightly recovered after CRT (83%).

The 3D BEP representation (Figure 5.5) also confirms the heterogeneous electrical activation in LBBB; it shows that slow speed or blocks of conduction areas are located in steep slopes (e.g. inter-ventricular transition, epicardium at LBBB) and the fast speed ones in flat zones (e.g. epicardial RV at LBBB). In LBBB, the speed in the LV endocardium (Figure 5.4b) is much slower and more uniform than at baseline (i.e. the slow speed zone is distributed all over the LV endocardium.) due to the malfunctioning of the PS. In the epicardial speed map, two high-speed areas can be identified at LBBB. The RV area can be interpreted from the fact that the right bundle branch is still healthy. The LV high-speed area is likely to come from a retrograde entrance into the PS. These two areas are separated by a slow speed region, which is mainly activated by the muscle fibers rather than by the PS. This inter-ventricular block of conduction is clearly visible (as a steep slope) in the 3D BEP (Figure 5.5).

The histogram of isochrones (Figure 5.3) reveals the effect of this inter-ventricular block in the electrical pattern at LBBB. Unlike at baseline (Figure 5.3a), the epicardial electrical activity is not synchronous in both ventricles. In fact, the RV epicardium (green bars in Figure 5.3b) is activated before both the LV endocardium and epicardium (blue and red bars in Figure 5.3b, respectively).

After CRT, the speed map of the endocardium (Figure 5.4c) shows a predominance of slow speed areas (in blue); however, it reveals some high-speed patches, which may support the hypothesis of a retrograde activation of the PS. Epicardial speed maps illustrate how the interventricular block, present in LBBB (identified as the blue zone that divides both ventricles), is replaced by a more heterogeneous zone, which suggests a partial correction of the inter-ventricular block. This correction is confirmed in the histograms of isochrones where the LV and RV epicardium (red bars in Figure 5.3c, respectively) are almost completely synchronized. The 3D BEP (Figure 5.5c) also supports these findings, presenting a smoother slope between earliest and latest activation areas (after initial lead-based activation) in CRT comparing to LBBB.

Corresponding EAM data representation and analysis for Pig#2 is provided as Supplementary material (Figure S1). Pig#2 can be categorized as a non-responder case since CRT produced a bad TAT recovery (-2.6%) and a non-complete electrical resynchronization (IVD_{CRT} of 7.3ms), as can be appreciated in Table 1. In this case the speed index reports an abnormal behavior after CRT since there is a higher amount of slow-speed tissue than at LBBB (79% and 98% for LBBB and CRT, respectively). The fact that the LV-TD_{CRT} is equal to zero indicates that the electrical wave arrives at the same time on the LV endocardium and epicardium. This is likely due to a sub-optimal lead positioning since both RV and LV leads were implanted in apical regions.

2) Infarcted pig model

For the infarcted pig models a radiologist analyzed a pre-operative DE-MRI to extract the LV segments affected by the scar, including the transmurality through the myocardium. This information is illustrated for Pig #3 in Figure 6 (for Pig #4, Figure S2 in Supplementary material).

Preprint version accepted to appear in IEEE Journal of Translational Engineering in Health and Medicine. Final version of this paper available at http://ieeexplore.ieee.org/xpl/RecentIssue.jsp?punumber=6221039

Pig #3 presents both a complete TAT recovery (100%) and a complete RV/LV electrical resynchronization (IVD_{CRT} = 0 ms) after CRT. As in the non-infarcted Pig#1, the LV-TD_{CRT} indicates that the LV epicardium activates electrically 6.75 ms before the LV endocardium because the LV and RV leads are located on the epicardium and the endocardium, respectively. Figure 6 illustrates the electrical activation pattern of Pig #3. In this case, the scar is located the antero-septal area with a transmurality of 52%. The viability of these segments is quite relevant to the electrical activation pattern, because it can alter the initial Purkinje activation area. This case presents a small scar influencing the anterior part of the left bundle branch of the Purkinje system. At baseline, the speed map in the endocardium (Figure 6.4a) shows the antero-septal area with a slower velocity of conduction than in the non-infarcted cases. Nevertheless, the epicardial electrical pattern remains faster and synchronous, as in the non-infarcted cases, probably due to the relatively limited scar transmurality. Furthermore, the speed index reveals a general reduction of the epicardial speeds at baseline in infarcted pigs compared to non-infarcted ones. This reduction at baseline is highly influenced by the scar transmurality (see Table 2): Pig#3 presents a transmurality of 52% and a 45% of slow speed tissue; and Pig#4 has a transmurality of 86% and a 61% of slow speed tissue. The 3D BEP at baseline (Figure 6.5) is quite illustrative since the scar zone is visualized as a large mountain with a steep slope.

At LBBB, an electrical pattern similar to the non-infarcted ones can be observed. The inter- and intra-ventricular electrical dyssynchrony at LBBB are clearly observed in the 2D BEP representation (Figure 6.2b), which are represented by substantially different activation times (earliest and latest LAT in red and blue, respectively). The endocardial speed map at LBBB shows a high-speed zone at the basal part of the LV septum (see top left in Figure 6.4b), which is induced by the transmural propagation of the RV electrical activation. The epicardial speed map (Figure 6.4b) also reveals the two high velocity peaks, one at each ventricle, separated by an area with slower conduction speed (blue area between both ventricles). This block can easily be identified on the 3D BEP (Figure 6.5). After CRT, the epicardial speed maps (Figure 6.4c) show how the electrical block between the two ventricles is partially corrected, even if it persists in the areas where the scar is located. The influence of this scar is highly visible at the endocardial level (Figure 6.4a), where scar-affected areas are consistently associated with slower speeds of conduction (blue areas). The partial correction of the inter-ventricular block is confirmed in the histogram of isochrones (Figure 6.3), where the LV and RV electrical activation is almost fully synchronized after CRT, even if the LV endocardium takes a bit longer to activate due to the scar presence. The 3D BEPs (Figure 6.5) demonstrate how the leads are located far away from the scar region and how the electrical activity surrounds it.

Corresponding EAM data representation and analysis for Pig #4 is provided as Supplementary material (Figure S2). This is an example in which a simple index such as the TAT recovery fails for assessing the benefits of the CRT. It presents a high TAT recovery (343%) but a poor RV/LV resynchronization that is reflected on a poor inter-ventricular dyssynchrony index (IVD_{CRT} = -12.25ms). Furthermore, the LV-TD_{CRT} shows a short LV transmural delay of 5.25ms, which suggest that the LV lead is correctly located. This case presents a huge scar (86% of transmurality) located in the antero-septal area. This scar location highly influences the PS activity, making the TAT at the endocardium larger than normal in baseline. Depending on the scar size, it can happen that inducing a LBBB will not introduce an additional delay. Due to the scar location (antero-septal and septo-apical areas), the RV lead was not exactly placed at the apex but close to a mid-inferior zone (apicality index of 0.35 in Table 1). This lead configuration induces a reduction of the global TAT but not an inter-ventricular synchronization.

V. DISCUSSION

We presented a complete framework to analyze intra- and inter-subject changes in electrical activation patterns, performing quantitative comparisons between data at different stages and different subjects. Our framework provides a set of tools whose usefulness is demonstrated to fully interpret individual patterns and improvements resulting from CRT. As shown by our experiments, EAMs are useful to study electrical activation patterns, partially due to the link between local activation times and the 3D anatomical information. However, they are very specific to each patient and acquisition, which makes their analysis non-trivial. Also, we proposed to embed to this mapping information the speed of conduction at each point for a better understanding of the electrical activation patterns. To our knowledge, this approach is innovative and highly complementary to the LAT information as it reveals areas of slow/fast conduction, harder to assess otherwise. We apply a classification based on the speed of conduction estimated, which reveals the influence of the Purkinje system onto the electrical activation pattern. It is therefore easier to identify either a block in the electrical propagation wave or a fast activation zone induced by the Purkinje system. Complementarily, the histogram of isochrones simultaneously relates the synchronicity of the electrical activation between endocardium and epicardium. This relation provides the amount of inter- (LV/RV) and intra-cavity (LV endocardium and epicardium) dyssynchrony, which is extremely relevant for evaluating CRT. Furthermore, large slopes in the histogram distribution clearly indicate the timing when the electrical activation joins the Purkinje system (e.g. in Figure 6.3 this happens between bins #8 and #9 in the LV endocardium).

We have illustrated the usefulness of these tools in fully controlled synthetic data and in an experimental model of induced LBBB with an implanted CRT device. QRS width and LV ejection fraction, in patients that present LBBB, are currently the indices recommended by clinical guidelines for selecting candidate patients to implant a CRT device [40]. However, these global indices do not provide enough information to understand the underlying activation pattern,

Preprint version accepted to appear in IEEE Journal of Translational Engineering in Health and Medicine. Final version of this paper available at http://ieeexplore.ieee.org/xpl/RecentIssue.jsp?punumber=6221039

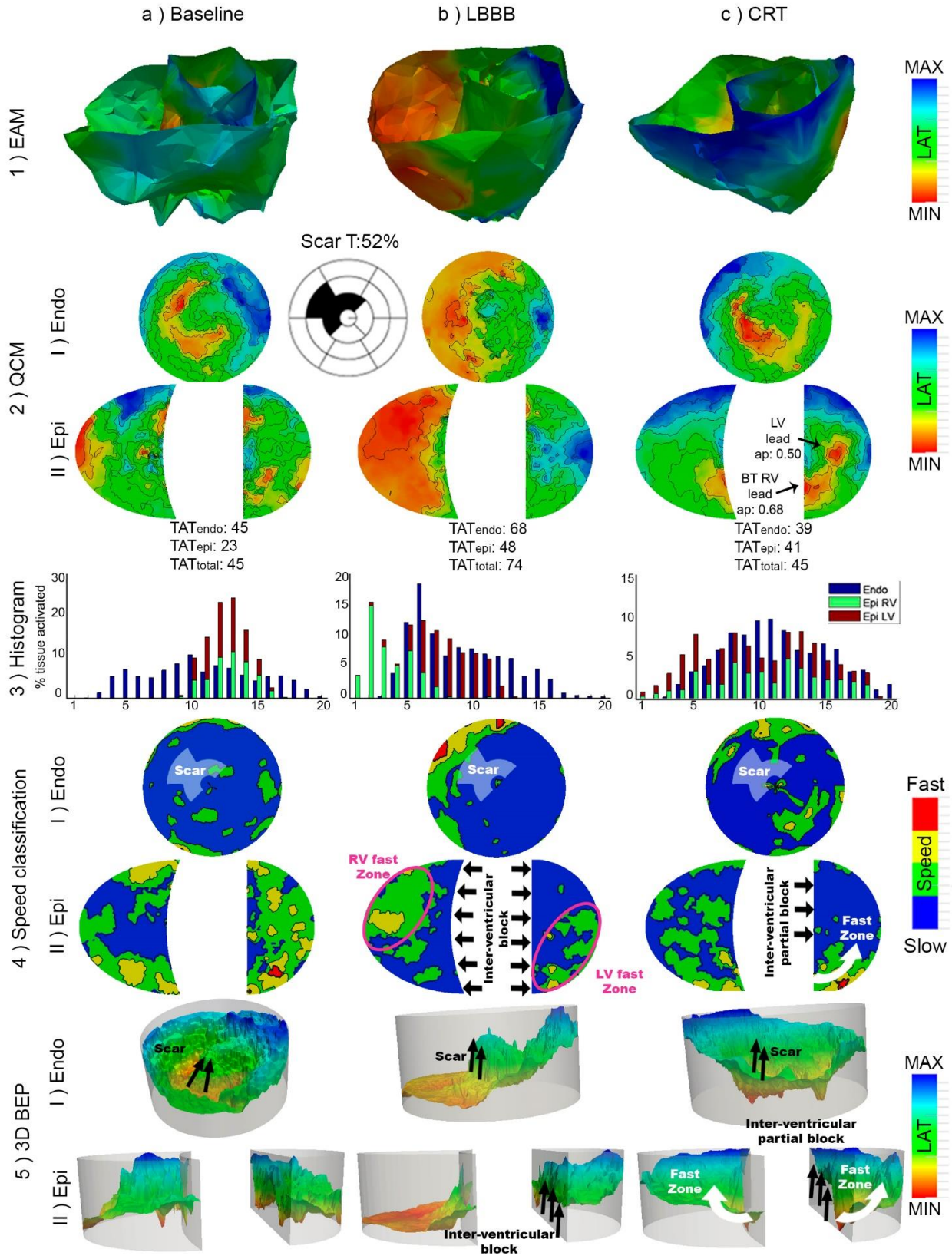

Figure 6. Infarcted case (*#3*). 1) Endocardial and epicardial EAMs 2) QCM of endo (LV) and epicardial (RV/LV) EAMs; BT RV: electrical breakthrough from the RV; 3) Histogram of isochrones (missing RV endocardium) 4) Speed classification from endo and epicardial velocity maps 5) 3D BEP from endo and epicardial QCM representations; Local activation time (LAT) values and speed scales are shown as min/max since they are different between each protocol stage.

Preprint version accepted to appear in IEEE Journal of Translational Engineering in Health and Medicine. Final version of this paper available at http://ieeexplore.ieee.org/xpl/RecentIssue.jsp?punumber=6221039

which is critical to reduce the number of non-responders to CRT. In the experimental model, EAMs provided a deeper understanding of the electrical activation pattern at different stages of the protocol, but required to be analyzed with advanced tools [2, 3]. Here, we point out the limits of a global index such as the TAT recovery (equivalent to the QRS width recovery), which can hide key factors as the dyssynchrony between both ventricles. Some authors [41] used the ventricular electrical uncoupling recovery (difference between averaged LV and RV local activation times), as a measure of RV/LV dyssynchrony. However, our inter-ventricular and transmural delay indices, extracted from the histogram of isochrones, are better suited for improving the assessment of the electrical recovery after CRT, since they also integrate the spatial distribution of the electrical activation. Additionally, the lead-based indices (e.g. apicality and geodesic distances) relate lead location with CRT response, which can be applied for testing different clinical hypothesis about optimal lead positioning. Our preliminary results quantitatively confirm the results by [32], namely that optimal pacing sites should target the RV lead close to the apex and the LV one distant from it.

The different EAM data representations presented in this paper rely in the accuracy of the initial quasi-conformal mapping. The main drawback of the QCM mapping is the sensitivity to the landmark selection, as was reported in [20, 21], but this issue has not induced aberrant results in the data processed in this paper. One limitation of the presented tools is the difficulty of acquiring good quality EAM data (a regularly distributed sufficient amount of points) in CRT patients due to the invasiveness of the contact-mapping procedures. Some authors [2] have acquired low-quality EAM data (reduced number of points) on CRT patients with a non-contact mapping system (i.e. basket of electrodes) for different lead configurations, enabling to qualitatively relate electrical indices with mechanical dyssynchrony information obtained from ultrasound images. The value of our study is to provide a general framework within which electrical activation patterns can be globally and locally analyzed in a quantitative way, independently on the acquisition system, to obtain electrical information. Therefore it could easily be adapted to new and promising non-invasive technologies to estimate electrical activation in the heart such as electrocardiographic imaging (ECGI) [42, 43, 44].

VI. Conclusions

The proposed methodology is applied for qualitatively and quantitatively analyzing electrical activation patterns extracted from EAMs. It provides a framework within which the local activation time is easily related with a surrogate for the velocity of conduction and the presence of any structural disease as the fibrotic tissue. Furthermore, we point out the limits of a global analysis of the EAMs. We show how the use of local indices, which integrates the spatial distribution of the electrical activation, improves the understanding of the electrical pattern. Although we show its usefulness on a swine model of LBBB/CRT, the whole pipeline can be applied for studying any kind of electrical activation disease. Future work will focus in the development of tools for relating both electrical and mechanical activation patterns.

VII. Acknowledgments

This study was partially funded by the Spanish Ministry of Science and Innovation (TIN2011-28067) and the Spanish Industrial and Technological Development Center (cvREMOD-CEN-20091044) and from the Seventh Framework Programme (FP7/2007-2013) for research, technological and demonstration under grant agreement VP2HF (nº 611823). The authors gratefully acknowledge the support of A. Doltra, N. Solanes, M. Rigol, L. Gabrielli, E. Silva (Hospital Clínic, Barcelona, Spain) and A. Barceló (Sorin group, Barcelona, Spain) on the experimental protocol.

References

[1] D.P. Zipes, A.J. Camm, M. Borggrefe et al. "ACC/aha/esc 2006 guidelines for management of patients with ventricular arrhythmias and the prevention of sudden cardiac death." *Europace*., vol. 8, pp. 746-837, 2006.

[2] S.G. Duckett O. Camara, M.R. Ginks et al. "Relationship between endocardial activation sequences defined by high-density mapping to early septal contraction (septal flash) in patients with left bundle branch block undergoing cardiac resynchronization therapy." *Europace*, pp. 99-106, 2012.

[3] E. Silva, B. Bijnens, A. Berruezo et al. "Integration of mechanical, structural and electrical imaging to understand response to cardiac resynchronization therapy." *Revista española de cardiología*, Eight edition, vol. 67(10), pp. 813-821, 2014.

[4] A. Auricchio, C. Fantoni, F. Regoli et al. "Characterization of left ventricular activation in patients with heart failure and left bundle-branch block." *Circulation*, vol. 109, pp. 1133-139, 2004.

[5] C. Herczku, A. Berruezo, D. Andreu et al. "Mapping data predictors of a left ventricular outflow tract origin of idiopathic ventricular tachycardia with V3 transition and septal earliest activation," *Circulation: Arrhythmia Electrophysiology*, vol. 5, pp. 484-491, 2012.

[6] J. Acosta, D. Penela, C. Herczku et al. "Impact of the Earliest Activation Site Location in the Septal Right Ventricular Outflow Tract for the Identification of Left vs Right Outflow Tract Origin of Idiopathic Ventricular Arrhythmias.", *Heart rhythm*, vol. 12, pp. 726-734, 2015.

[7] A. Berruezo, J. Fernández-Armenta, D. Andreu et al. "Scar dechannelling: New method for scar-related left ventricular tachycardia substrate ablation." *Circulation: Arrhythmia and Electrophysiology*, vol. 8, pp. 326-336. 2015.

[8] J. Fernández-Armenta, A. Berruezo, D. Andreu er at. "Three-dimensional architecture of scar and conducting channels based on high resolution ce-cmr: Insights for ventricular tachycardia ablation." *Circulation: Arrhythmia and Electrophysiology*, vol. 6, pp. 528-537. 2013.

[9] A. Codreanu, F. Odille, E. Aliot et al. "Electroanatomic characterization of post-infarct scars comparison with 3-dimensional myocardial scar reconstruction based on magnetic resonance imaging." *Journal of American College of Cardiology*, Vol. 52, pp. 839-842. 2008.

[10] A.R. Porras, G. Piella, A. Berruezo et al. "Interventional endocardial motion estimation from electroanatomical mapping data: application to scar characterization." *IEEE Journal on Transaction Biomedical Engineering*, vol. 60, pp. 1217-224, 2013.

[11] A.R. Porras, G. Piella, A. Berruezo et al. "Pre- to intra-operative data fusion framework for multimodal characterization of myocardial scar tissue." *IEEE Journal of translational engineering in health and medicine*. vol. 2. 2014

[12] R. Karim, Y. Ma, R.J. Housden et al, "Surface flattening of the human left atrium and proof-of-concept clinical applications."

Preprint version accepted to appear in IEEE Journal of Translational Engineering in Health and Medicine. Final version of this paper available at http://ieeexplore.ieee.org/xpl/RecentIssue.jsp?punumber=6221039

Computerized Medical Imaging and Graphics, vol. 38, no. 4, pp. 251-266, 2014.

[13] C. Tobon-Gomez, M.A. Zuluaga, H. Chubb et al. "Standardized unfold map of the left atrium: regional definition for multimodal image analysis," *Journal of Cardiovascular Magnetic Resonance*, vol. 17, pp. 41, 2015.

[14] G. Auzias, J. Lefèvre, A. Le Troter et al. "Model-Driven Harmonic Parametrization of the Cortical Surface: HIP-HOP," *IEEE Transactions on Medical Imaging*, vol. 32, pp. 873-887, 2013.

[15] P.A. Yushkevich, H. Zhang, J.C. Gee et al. "Continuous medical representation for harmonic structures," *IEEE Transactions on Medical Imaging*, vol. 25, pp. 1547-564, 2006.

[16] S. Vera, M.A. Ballester, D. Gil et al. "Anatomical parametrization for volumetric meshing of the liver," *SPIE Medical Imaging*, vol. 9034, 2014.

[17] S. Vera, M.A. Ballester, D. Gil et al. "A novel cochlear reference frame based on the laplace equation." *Computed Assisted Radiology and Surgery*, 2015.

[18] K.C. Lam, X. Gu, L. Lui et al, "Genus-one surface registration via Teichmüller extremal mapping," in *MICCAI*, vol. 3, pp.25-32, *2014*.

[19] W. Zeng, D. Samaras, X. Gu, "Ricci flow for 3D shape analysis" in *IEEE Pattern Analysis and Machine Intelligence*, vol. 32, pp. 662-677, 2010.

[20] D. Soto-Iglesias, C. Butakoff, D. Andreu et al., "Evaluation of different mapping techniques for the integration of electro-anatomical voltage and imaging data of the left ventricle." *Functional imaging and modeling of the heart*, LNCS 7945, pp. 391-399. 2013.

[21] D. Soto-Iglesias, C. Butakoff, D. Andreu et al., "Integration of electro-anatomical and imaging data of the left ventricle using quasi-conformal mapping.", submitted

[22] D. Soto-Iglesias, N. Duchateau, C. Butakoff et al. "Analyzing electrical patterns in an experimental swine model of dyssynchrony and CRT." *Computing in cardiology*, pp. 623-626, 2013.

[23] L. Jing, C.M. Haggerty, J.D. Suever et al, "Patients with repaired tetralogy of Fallot suffer from intra- and inter-ventricular cardiac dyssynchrony: a cardiac magnetic resonance study." In *Journal of Cardiovascular Imaging*, vol. 12, pp.1333-343, 2014.

[24] N. Duchateau, B. Bijnens, J. D'hooge et al. "Three-dimensional assessment of cardiac motion and deformation." *Shiota T, ed: 3D echocardiography*, 2nd edition. CRC, press, pp. 201-213, 2013.

[25] K. Vernooy, C.J. Van Deursen, M. Strik et al, "Strategies to improve cardiac resynchronization therapy." in *Nature review cardiology*, vol.11, pp. 481-493, 2014.

[26] G.B. Bleeker, J.J. Bax, J.W. Fung et al, "Clinical versus echocardiographic parameters to assess response to cardiac resynchronization therapy." in *American Journal of Cardiology*, vol.97, pp. 260-3, 2006.

[27] J. Singh, H.U. Klein, D.T. Huang et al, "Left ventricular lead position and clinical outcome in the multi-center automatic defibrillator implantation trial-cardiac resynchronization therapy (MADIT-CRT) trial." in *Circulation*, vol 123, pp. 1159-166, 2011.

[28] M. Gold, A. Auricchio, J.D. Hummel et al, "Comparison of stimulation sites within left ventricular veins on the acute hemodynamic effects of cardiac resynchronization therapy" *Heart Rhythm*, vol. 2, pp. 376-381, 2005.

[29] L. Saxin, B. Olshansky, K. Volosin et al, "Influence of left ventricular lead location on outcomes in the COMPANION study." *Journal of Cardiovascular Electrophysiology*, vol. 20, pp. 764-768, 2009.

[30] C Tobon-Gomez, N Duchateau, R Sebastian et al. "Understanding the mechanisms amenable to CRT response: from pre-operative multimodal image data to patient-specific computational models." *Medical & biological engineering & computing*, vol. 51, pp. 1235-250.2013.

[31] N. Smith, A. de Vecchi, M. McCormick et al. "euHeart: personalized and integrated cardiac care using patient-specific cardiovascular modelling." *Interdace Focus*, vol. 1, pp. 349-364, 2011.

[32] P. Huntjens, J. Walmsley, S. Ploux et al, "Influence of left ventricular lead position relative to scar location on response to cardiac resynchronization therapy: a model study." in *Europace*, vol. 16, pp. 62-68, 2014.

[33] J. Lumens, S. Ploux, M. Strik et al, "Comparative electromechanical and hemodynamic effects of left ventricular and biventricular pacing in dyssynchronous heart failure." in *Journal of American College of Cardiology*, vol. 62, pp. 2395-403, 2013.

[34] J. MacQueen, "Some methods for classification and analysis of multivariate observations." in *Proceedings of the Fifth Berkeley Symposium on Mathematical Statistics and Probability*, vol. 1: Statistics, pp.281-297, 1967.

[35] C. Ypenburg, R.J. van Bommel, V. Delgado, et al. "Optimal left ventricular lead position predicts reverse remodeling and survival after cardiac resynchronization therapy." *Journal of the American College of Cardiology*, vol. 52, pp.1402–409, 2008.

[36] R.T. Murphy, G. Sigurdsson, S. Mulamalla, et al. "Tissue synchronization imaging and optimal left ventricular pacing site in cardiac resynchronization therapy." *American Journal of Cardiology*, vol. 97, pp. 1615–621, 2006.

[37] M. Rigol, N. Solanes, J. Fernandez-Armenta et al, "Development of a swine model of left bundle branch block for experimental studies of cardiac resynchronization therapy." in *Journal of Cardiovascular Translational Research*, vol. 6, pp. 616-622, 2013.

[38] National research council, "Guide for the Care and use of Laboratory Animals: Eight edition", *Washington DC: The National Academic Press*, 2011.

[39] P. Houthuzien, F.A. Bracke, B.M. Van Gelder. "Atrioventricular and interventricular delay optimization in cardiac resynchronization therapy: physiological principles and overview of available methods." *Heart failure reviews*, vol. 16, pp. 263-276, 2010.

[40] M. Brignole, A. Auricchio, G. Baron-Esquivias et al, "2013 ESC guidelines on cardiac pacing and cardiac resynchronization therapy: the Task Forze on cardiac pacing and resynchronization therapy of the European Society of Cardiology (ESC). Developed in collaboration with the European Heart Rhythm Association (EHRA). " in *Europace*, vol. 15, pp. 1070-118, 2013.

[41] R. Eschalier, S. Ploux, J. Lumens et al. "Detailed analysis of ventricular activation sequences during right ventricular apical pacing and left bundle branch block and the potential implications for cardiac resynchronization therapy." *Heart Rhythm*, vol. 12, pp 137-143, 2015.

[42] R. Dubois, A.J. Shah, M. Hocini et al. "Non-invasive cardiac mapping in clinical practice: Application to the ablation of cardiac arrhythmias." *Journal of Electrocardiology*, vol. 48, pp. 966-974, 2015.

[43] P. Jia, C. Ramanathan, R.N. Ghanem et al, "Electrocardiographic imaging of cardiac resynchronization therapy in heart failure: observation of variable electrophysiologic responses." *Heart rhythm*, vol. 3, pp. 296-310, 2006.

[44] S. Ploux, J. Lumens, Z. Whinnett et al. "Noninvasive electrocardiographic mapping to improve patient selection for cardiac resynchronization therapy: beyond QRS duration and left bundle branch block morphology.", *Journal of the American College of Cardiology*, vol. 61, pp. 2435-443, 2013.

Preprint version accepted to appear in IEEE Journal of Translational Engineering in Health and Medicine. Final version of this paper available at http://ieeexplore.ieee.org/xpl/RecentIssue.jsp?punumber=6221039

VIII. SUPPLEMENTARY MATERIAL

Figure S1 shows the electrical activation pattern of the non-infarcted and CRT non-responder Pig #2 since CRT produced a poor TAT recovery (-2.6%) and a non-complete electrical resynchronization (IVD_{CRT} = 7.3ms), as can be seen in Table 1. As for Pig #1 (a responder case), the 2D BEP shows a homogeneous and faster activation of the endocardium and epicardium at baseline compared to LBBB. The speed maps (Figure S1.4) reveal the presence of Purkinje-based activation at both endocardium and epicardium levels at baseline, in the form of a transition zone between slow and fast speed areas (blue and green in Figure S1.4, respectively), which is not present neither at LBBB or CRT. The 3D BEP (Figure S1.5) illustrates the inter-ventricular block induced after LBBB at the epicardial level, isolating two high speed areas (one at each ventricle) that are visible as flat zones in the 3D BEP. The histograms of isochrones (Figure S1.3) clearly show the inter-ventricular electrical dyssynchrony in the epicardium. At LBBB, it can be seen how the RV epicardium (green bars in Figure S1.3) is activated not only before the LV epicardium but also before the LV endocardium. At CRT, the epicardial 2D BEP (Figure S1.2) allows an easy identification of the lead placement; in this case, the LV lead is placed at an apical position (apicality index of 0.79) so it overlaps with the electrical RV breakthrough (apicality index of 0.89), reducing the benefits of bi-ventricular pacing to only one lead. The speed maps (Figure S1.4) show how this CRT lead configuration provides slower speeds than even at LBBB (i.e. more blue areas in Figure S1.4). Even if the histogram of isochrones after CRT (Figure S1.3) shows an improvement of the inter-ventricular dyssynchrony compared to LBBB (i.e. the IVD is improved from 18 ms to 7.3 ms), we can still visually observe dyssynchrony at the end of the epicardial activation (green and blue bars in Figure S1.3). The 3D BEP (Figure S1.5) also depicts how the inter-ventricular block is still present after CRT, which indicates that this lead configuration is not appropriate for improving the LBBB abnormal electrical patterns.

Figure S2 shows the electrical activation pattern of the infarcted and CRT non-responder Pig #4. This case presents a big scar (86% of transmurality) located in the antero-septal area, which highly influences the PS activity. The presence of the scar produces a TAT at the endocardium larger than normal in baseline (52 ms); in fact it is the same than the one at LBBB. Despite equal TATs, the 2D BEP (Figure S2.2) depicts a more uniform activation at baseline than at LBBB. It also reveals the effect of the scar on the baseline electrical activation pattern. It can be seen that the first Purkinje-based activation area (antero- and infero-septal wall) differs with respect to the non-infarcted one (it presents a bigger green zone instead of a red one, Figure S1.2 in contrast to Figure S2.2). The scar location can be more clearly located on the speed maps (Figure S2.4) and 3D BEP (Figure S2.5). The scarred segments are consistently associated to slow speed areas (blue zones in Figure S2.4) in the epicardial speed map. Differences between the anterior and inferior LV wall indicate how the scar is influencing the anterior PS branch but not the inferior one. The electrical block induced by the scar is also clearly visible on the 3D BEP (Figure S2.5.I), where the steepest slope is located on the scarred area. In spite of the scar transmurality (86%), the baseline epicardial activity remains fast and uniform (Figure S2.4) and the electrical block is not visible on the 3D BEP (Figure S2.5). The histogram of isochrones (Figure S2.3) reveals how the scar highly influences the initial bins of the LV endocardial activity by reducing its speed of conduction (i.e. very low % of activated tissue on bins 1-5). Similar to the other cases, the inter-ventricular dyssynchrony can be observed on the histogram of isochrones (Figure S2.3b). The speed maps shows a transition zone (anterior zone of LBBB endocardial speed map, Figure S2.4b) between the scar area and the healthy tissue, which indicates how the scar induces a block in the electrical propagation wave forcing it to surround the infarcted area. At the epicardial level, the velocity is much slower than in baseline but the inter-ventricular block is better observed on the 3D BEP (Figure S2.5). At CRT, the 2D BEP demonstrates how both the LV and the RV breakthroughs are located on the LV wall. This is consequence of the scar location, which affects the apical part of the septum with a transmurality of 86%, making the RV apex a non-adequate RV lead location. Therefore, the RV lead was placed on a mid-inferior zone of the RV endocardium. Such a lead configuration creates a faster LV depolarization that reduces the TAT but it does not correct the inter-ventricular dyssynchrony, as can be seen in the histogram of isochrones (Figure S2.3c). The fact that the speeds are of the same order at the three stages (i.e. the presence of all the clusters on the endocardial speed maps, Figure S2.4) indicates that the baseline speed has been substantially decreased by the presence of the scar. In particular, a huge scar located on septal locations can influence on the PS making the velocity of conduction similar to that on LBBB.

Preprint version accepted to appear in IEEE Journal of Translational Engineering in Health and Medicine. Final version of this paper available at http://ieeexplore.ieee.org/xpl/RecentIssue.jsp?punumber=6221039

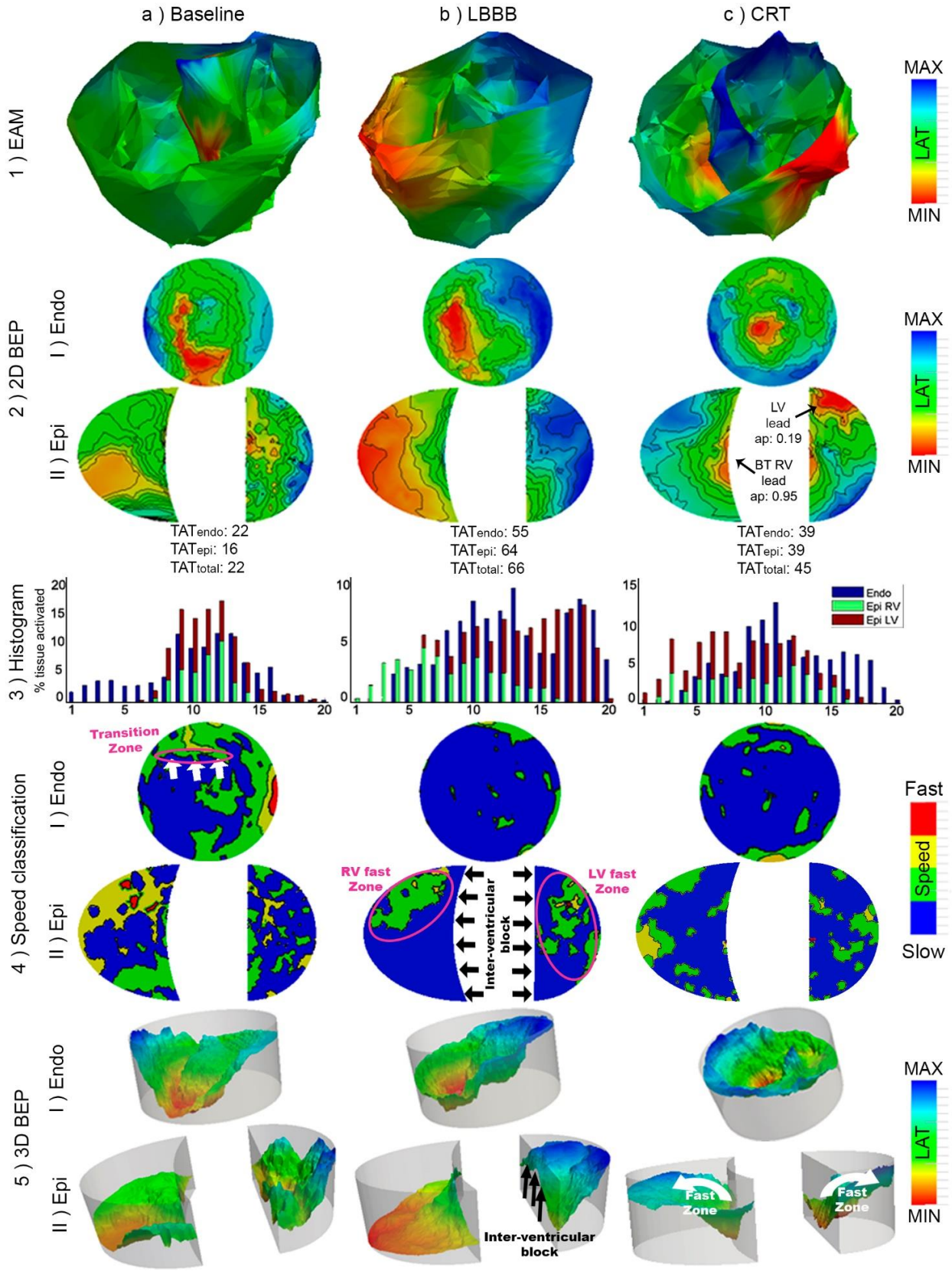

Figure S1. Non-infarcted case (#2). 1) Endocardial and epicardial EAMs 2) QCM of endo (LV) and epicardial (RV/LV) EAMs; BT RV: electrical breakthrough from the RV; 3) Histogram of isochrones (missing RV endocardium) 4) Speed classification from endo and epicardial velocity maps 5) 3D BEP from endo and epicardial QCM representations; Local activation time (LAT) values and speed scales are shown as min/max since they are different between each protocol stage.

Preprint version accepted to appear in IEEE Journal of Translational Engineering in Health and Medicine. Final version of this paper available at http://ieeexplore.ieee.org/xpl/RecentIssue.jsp?punumber=6221039

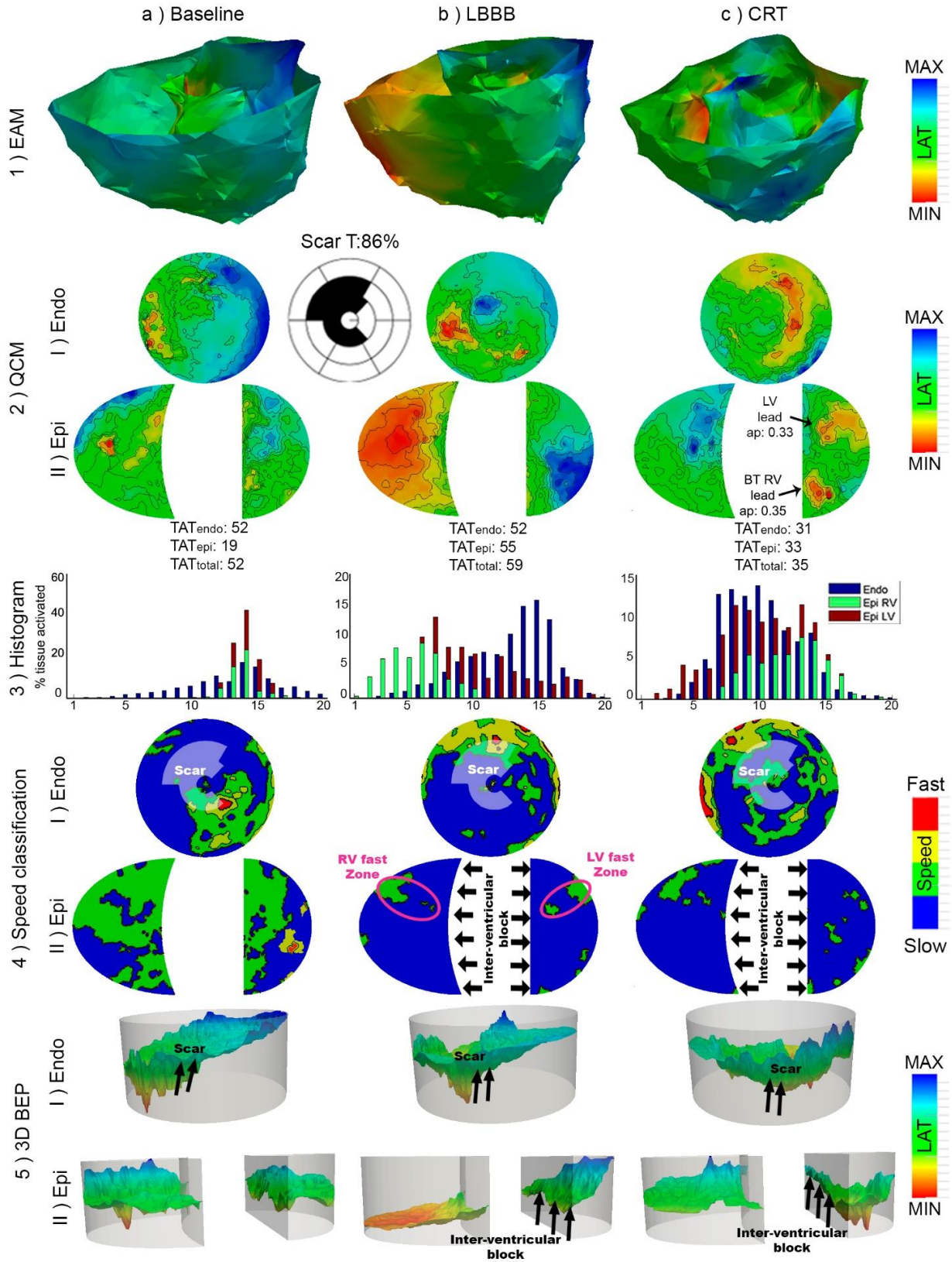

Figure S2. Infarcted case (*#4*). 1) Endocardial and epicardial EAMs 2) QCM of endo (LV) and epicardial (RV/LV) EAMs; BT RV: electrical breakthrough from the RV; 3) Histogram of isochrones (missing RV endocardium) 4) Speed classification from endo and epicardial velocity maps 5) 3D BEP from endo and epicardial QCM representations; Local activation time (LAT) values and speed scales are shown as min/max since they are different between each protocol stage.

Preprint version accepted to appear in IEEE Journal of Translational Engineering in Health and Medicine. Final version of this paper available at http://ieeexplore.ieee.org/xpl/RecentIssue.jsp?punumber=6221039

Index		Unit	Purpose
2D BEP		Map	Electrical activation pattern analysis
3D BEP		Map	Joint analysis of electrical and speed activation pattern
Speed map		Map	Tissue classification based on the speed of conduction. Identification of transition zones
Histogram of isochrones		Map	Relation of LV endocardial and bi-ventricular epicardial electrical activation pattern.
TAT related indices	Δ_{Base}	Scalar	Analyze changes in the total activation time between different stages.
	Δ_{CRT}		
	$TAT_{Recovery}$		
Histogram related indices	IVD	Scalar	Relation between inter- and intra-ventricular dyssynchrony.
	TD		
Speed index		Scalar	Percentage of tissue activated within each speed cluster
Apicality index		Scalar	LV/RV leads location with respect to apical places
Leads distances	Leads	Scalar	Distance between LV/RV leads
	LAZ		Distance from LV lead at CRT to the latest activated zone in LBBB

Table S1. Summary of the indices proposed on this work, organized into map-related (blue), activation-related indices (green) and therapy-related indices (orange).